PCCP

PAPER

View Article Online
View Journal | View Issue

# An energetic evaluation of dissolution corrosion capabilities of liquid metals on iron surface

Cite this: *Phys. Chem. Chem. Phys.*, 2014, **16**, 16837

Yichun Xu,[a] Chi Song,[a] Yange Zhang,[a] C. S. Liu,*[a] B. C. Pan[b] and Zhiguang Wang[c]

Received 25th March 2014,
Accepted 16th June 2014

DOI: 10.1039/c4cp01224k

www.rsc.org/pccp

Using first principles calculations, dissolution corrosion of liquid metals on iron surfaces has been investigated by calculating adsorption energies of metal atoms in the liquid phase on the surface and escape energies of surface Fe atoms. The adsorption energies, characterizing the stability of the adsorbed atoms on the investigated surfaces, show that Bi is more stable than Pb and Au. The escape energies, representing the energy required for an Fe atom to escape from the surface, show that adsorbed Pb makes surface Fe atoms escape more easily than Bi and Au. The combination of adsorption energy and escape energy indicates that the corrosion capabilities of liquid metals decrease in the order Bi > Pb > Au. This is further proved by the investigation of surface properties, such as inter-layer distance, magnetic momentum and charge density difference. The results are consistent with experimental results that Fe can be corroded more severely in Bi than in Pb. In the case of liquid alloys, chemical proportions of compositions are incorporated to evaluate the corrosion capabilities of Pb–Bi eutectic (LBE) and Pb–Au eutectic (LGE). It is found that LBE has more severe corrosion capability than LGE. The energetic calculation is further developed in evaluating the effect of alloying elements in popular steels on the dissolution corrosion. The results indicate that Si, V, Nb and Mo may mitigate the dissolution corrosion of martensite steels in liquid Pb, Bi and Au.

## 1 Introduction

Heavy liquid metals are promising candidates for core coolants and high-power spallation targets in accelerator driven systems (ADSs), because of their low melting point, low vapor pressure, high neutron yield and good heat removal.[1–3] For example, liquid Pb–Bi eutectic (LBE) has been generally accepted as a good candidate and studied by a number of laboratories worldwide for several years. Liquid Pb–Au eutectic (LGE) was recently validated as an alternative candidate due to its lower chemical toxicity and similar neutron production, with less polonium as compared to mercury and LBE.[4] However, the compatibility of structural materials, many stainless steels, with the liquid metals is a critical problem in the development of ADS.[5–7] A series of experiments has shown that most steels are attacked by dissolution corrosion at low oxygen content (especially less than $1 \times 10^{-8}$ wt%), and oxidation corrosion at high oxygen concentration (larger than $1 \times 10^{-6}$ wt%).[8–12] Prior studies show that metallic inhibitors, Zr and Ti, can inhibit the corrosion of steels by reacting with minor constituents of steels, nitrogen and carbon to form inert and adherent surface layers of ZrN, TiN or TiC.[13–15] Recently, non-metallic oxygen has been found to be an effective inhibitor by reacting with the major components of steels to form a protective oxide layer.[16,17] However, the nitrides and carbides are controlled by the diffusion of nitrogen and carbon and some of them are brittle and tend to spall.[17] On the other hand, the oxide layer thickness depends strongly on the oxygen concentration by the active oxygen control technique,[12] compositions and microstructures of steels,[11,18] and temperature and velocity of liquid metals.[9,11] Meanwhile, the ideal protective oxide layer should be pore-free, crack-free, stress-free at operating temperatures, and resistant to spalling or damage during cooling or heating. For practical heavy liquid metal systems, it is nearly impossible to attain such an ideal protective layer throughout the varying environments. These drive people to explore a different way to mitigate dissolution corrosion.

As we know, dissolution corrosion depends not only on the compositions of liquid metals, but also on the components of the materials. Weeks in the 1960s found that the Fe solubility decreases with increasing Pb fraction in liquid Pb–Bi.[19] This indicates that Bi has more severe corrosion capability than Pb, which was further proved by comparing the Ni and Cr solubility in liquid Pb and Pb–Bi alloy[19] and various steels in liquid Pb and Bi.[11,20] It is also found that Cr is corroded more easily than Fe in liquid Pb–Bi. According to the observations of CICLAD and CORRONa, the dissolution rates of T91 and Eurofer97 in Pb alloys are higher than those in Na at the same temperature.[21]

[a] *Key Laboratory of Materials Physics, Institute of Solid State Physics, Chinese Academy of Sciences, P. O. Box 1129, Hefei 230031, P. R. China. E-mail: csliu@issp.ac.cn; Fax: +86 551 65591434; Tel: +86 551 65591062*
[b] *National Laboratory for Physical Sciences at Microscale and Department of Physics, University of Science and Technology of China, Hefei 230026, P. R. China*
[c] *Institute of Modern Physics, Chinese Academy of Sciences, Lanzhou 730000, P. R. China*

Recently, both martensite T91 (body-centered cubic, bcc) and austenite SS316 (face-centered cubic, fcc) steels are corroded more severely in LGE than in LBE from PSI (the Paul Scherrer Institute, Switzerland) under identical conditions, including temperature, velocity and corrosion duration. Some components in the SS316 are dissolved significantly in LGE, such as Cr, Ni and Mn,[22] which is also observed in ref. 23–25. These experimental results indicate that both liquid metals and material components play important roles in dissolution corrosion. However, it is a costly and time-consuming job to select the best candidate from the massive materials for the ADS project by experiments.

With the development of computers, computational methods have been generally accepted as a good approach to obtain atomic information.[26–35] On the microscopic scale, the dissolution corrosion is a physico-chemical interaction between liquid metals and substrate surfaces. Similar to the corrosion at $Fe_3O_4$ surfaces,[26] we consider the adsorbing (or deposition) process of metal atoms in the liquid phase, and the escape process of surface Fe atoms. During the adsorption process, metal atoms in the liquid phase should be chemically stably adsorbed on the surface through temporary physical adsorption. Stable adsorption represents high adsorbing strength for the adsorbed atom (adatom) on the surface, which is related to its probability of adsorption. Meanwhile, the adatom causes the electrons to be re-distributed around the surface atoms. This will modify the surface stability and the escape possibilities of surface atoms. Consequently, it is speculated that the dissolution corrosion capabilities of liquid metals can be evaluated in terms of (1) adsorption energy related to the possibility of adsorbing atoms,[27,28] and (2) escape energy of the substrate atoms on the surface related to the surface stability.[29–31] In the case of liquid alloys, the dissolution corrosion has to be considered for each composition, such as Pb and Au in LGE, and Pb and Bi in LBE. On the alloy doped surfaces, interactions between liquid metals and alloy atoms are incorporated to examine the effects of alloying elements on the corrosion.

In this paper, we perform first principles calculations to evaluate the dissolution corrosion capabilities of liquid metals on the Fe surface by adsorption energy and escape energy. They are also double-checked by the surface properties, including inter-layer distance, magnetic momentum and charge density difference. In addition, alloys (Al, Si, V, Cr, Mn, Ni, Cu, Nb and Mo) in current popular steels are doped on the surface to explore their effects on the corrosion resistance of steels in liquid metals. This preliminary study is the first step towards understanding dissolution corrosion in liquid metals, although the extrapolation to real systems is complicated due to the presence of oxygen, impurities, defect sites and grain boundaries.

## 2 Computational details

The present calculations are based on the density functional theory (DFT), as implemented in the Vienna Ab initio Simulation Package (VASP).[36,37] The exchange–correlation energy is described by Perdew–Burke–Ernzerhof (PBE) form[38] within the spin polarized version of generalized gradient approximation (GGA). The electron–ionic core interactions are described by the projector augmented wave (PAW) potentials.[39,40] A plane-wave basis with energy cutoff of 500 eV is used to expand the electronic wave functions. The Brillouin zone integrations are performed on a special $k$-points mesh, $8 \times 8 \times 8$ for the bcc structure bulk, generated by the Monkhorst–Pack scheme.[41] Spin polarized calculations were conducted, due to the magnetic nature of Fe. To accelerate the convergence, the first order Methfessel–Paxton method with a Fermi surface smearing of 0.2 eV is adopted. With the above parameters, the lattice constant of bulk Fe with a bcc structure is optimized to be 2.831 Å. This value is consistent with the experimental data and other DFT calculations.[42,43]

Clean surfaces are modeled by cleaving the relaxed bcc-Fe bulk along the (001), (110) and (111) Miller planes. The three low index surfaces are usually taken into account to evaluate the dissolution corrosion capabilities of liquid metals.[44,45] For the (001) surface, different surface unit cells are considered to preset various coverages of adsorbed atoms and escaped Fe atoms (or vacancies). A slab consists of a $2 \times 2$ unit cell with 9 atomic layers, or a $3 \times 3$ unit cell with 5 atomic layers. For (110) and (111) surfaces, slabs are initiated by a $3 \times 3$ unit cell with 5 atomic layers and 4 atomic layers[46] in Fig. 1, respectively. Periodic slabs are separated by a 14 Å vacuum in the direction perpendicular to the surface. The upper surface is used to mimic the surface of interest, and the bottom surface is fixed, according to previous simulations.[26] All the surfaces are fully optimized until the forces on each atom in the corresponding slabs are less than 0.01 eV $Å^{-1}$. The sampling of the Brillouin zone for the $2 \times 2$ surface cells is conducted with a $k$-point mesh of $8 \times 8 \times 1$, while for $3 \times 3$ surface cells with a $k$-point mesh of $5 \times 5 \times 1$ generated automatically using the Monkhorst–Pack method. A series of test calculations show that our calculations with the aforementioned parameters are precise enough to obtain energetic information of the slab to within 0.03 eV.

Liquid metal adsorbed surfaces are considered by adsorbing Pb, Bi or Au atoms on the optimized clean surfaces at the different high-symmetry sites to determine the lowest energy configuration. As labeled in Fig. 1, Hollow (H), Bridge (B) and the Top (T) positions are considered on the (001) surface. Meanwhile, Long-Bridge (LB), Short-Bridge (SB) and Top sites on (110), and Bridge and Top sites on the (111) surface are examined. The configurations with the lowest energy are then utilized to analyze the energies in this paper. For the (001) surface, different coverages of adsorbed atoms are initiated to investigate the coverage dependence of the dissolution corrosion. One adatom at the $2 \times 2$ and $3 \times 3$ unit cell corresponds to coverage ($\theta$) of 1/4 and 1/9 ML, respectively. Two adatoms on the $2 \times 2$ unit cell corresponds to $\theta$ = 1/2 ML, and five adatoms on the $3 \times 3$ unit cell represents $\theta$ = 5/9 ML, as shown in Fig. 2. For the slabs with $2 \times 2$ unit cell surfaces, the bottom three layers are fixed, while the adsorbed atoms and Fe-atoms in the top six layers are relaxed, as shown in Fig. 3(a). For the slabs with $3 \times 3$ unit cell surfaces, Fe-atoms on the bottom two layers are fixed and the other atoms are relaxed, as shown in Fig. 1.

 

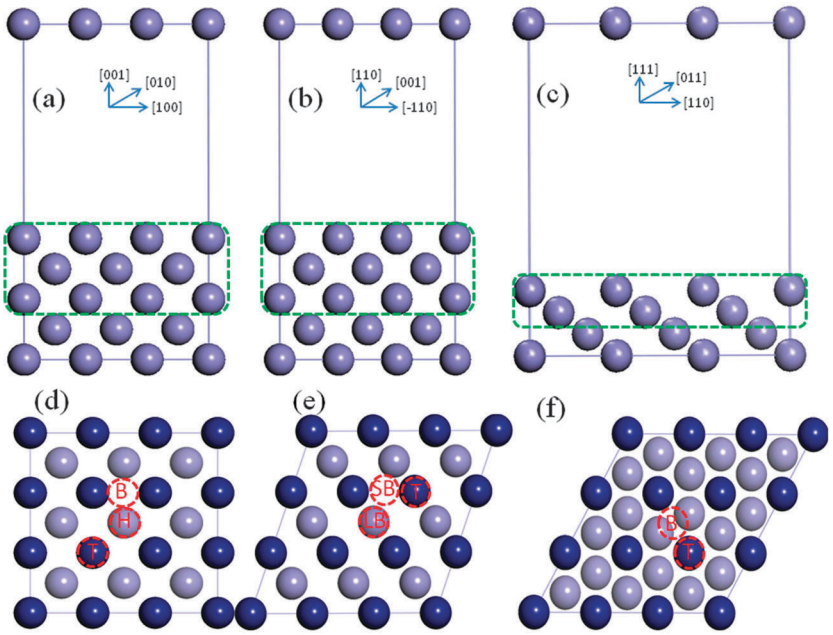


Fig. 1 The Fe-slab with (001) surface on (a), (110) surface on (b) and (111) surface on (c), and their corresponding overview on (d), (e) and (f), respectively. Dashed squares show relaxed atomic layers in different slabs. The dark blue balls are surface Fe atoms, and the light blue balls are Fe atoms in the second layer. Dashed circles represent the high-symmetry positions for adatoms on different surfaces, such as Hollow (H), Bridge (B), Top (T), Long-Bridge (LB) and Short-Bridge (SB).

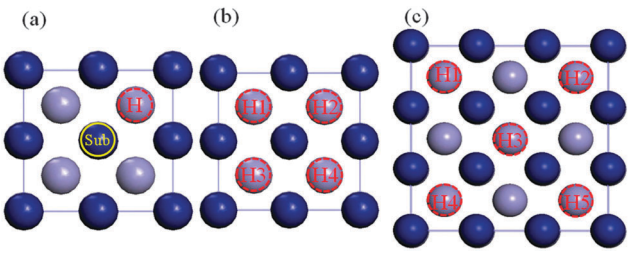


Fig. 2 Different coverage of adatoms on the Fe(001) surface with 2 × 2 and 3 × 3 unit cell. (a) 1/4 ML coverage of adatom and alloyed atom (labeled as Sub); (b) 1/2 ML coverage of adatoms, *i.e.* H1 and H4, or H2 and H3 is more stable than other assemblies; (c) 5/9 ML coverage of adatoms.

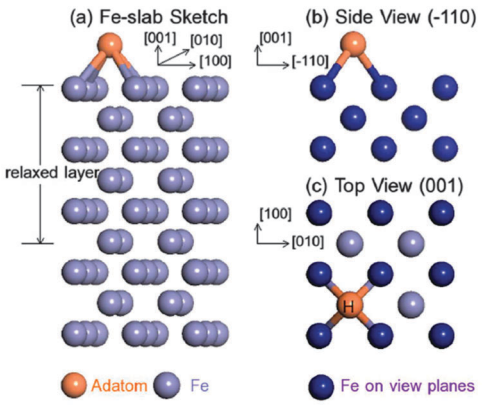


Fig. 3 (a) Structure of the Fe-slab with adsorbed atom on the hollow position; (b) side view of the structure on the (−110) plane; (c) top view of the structure on the (001) surface. The adsorbed atom at the hollow position is labeled as H.

# 3 Results and discussion

To evaluate the dissolution corrosion capabilities of liquid metals on Fe surfaces, we calculate adsorption energy of atoms from the liquid phase and escape energy for surface Fe atoms. The energetic evaluation is further checked by another distinct method, measuring the inter-layer distances, magnetic moments of surface Fe atoms and charge density differences at the interface of liquid metals/Fe(001). Finally, nine alloying elements are considered to explore their effects on the dissolution corrosion of liquid metals on alloy doped surfaces.

## 3.1 Dissolution corrosion capabilities of liquid metals

As mentioned above, we simultaneously consider the adsorbing process of metal atoms from the liquid phase and the escape process of surface Fe atoms in energetic space. According to previous calculations,[27–31] these two processes are described by the adsorption energy of adatoms, $E_{ads}$, and the escape energy of surface Fe atoms, $E_{esp}$. $E_{ads}$ is defined as:

$$E_{ads} = E_{slab}^{ada} - E_{slab} - \mu^{ada}, \quad (1)$$

where $E_{slab}^{ada}$ and $E_{slab}$ are the total energies of the slab with and without an adsorbed atom, respectively, and $\mu^{ada}$ is the chemical potential of the adsorbed atom. $\mu^{ada}$ is very close to the energy per atom of the most stable condensed phase of the adsorbed atom at 0 K, if the temperature dependence of the free energy and the latent heat of fusion is neglected.[27] $E_{esp}$ is defined as:

$$E_{esp} = E_{slab-1}^{ada} + E_{Fe} - E_{slab}^{ada}, \quad (2)$$

where $E_{slab}^{ada}$ is the total energy of the slab with adatoms from the liquid phase, $E_{slab-1}^{ada}$ is the total energy of the slab with adatoms and one surface Fe atom escaped from the surface, and $E_{Fe}$ is the energy of an isolated Fe atom. According to the above definitions, the negative $E_{ads}$ represents an exothermic process, and the adsorbing process occurs easily. On the contrary, a positive value indicates an endothermic process. The $E_{esp}$ represents the energy required for an Fe atom to escape from the surface. The lower the $E_{esp}$, the more easily the Fe atom escapes.

According to eqn (1), the $E_{ads}$ for adatoms at different positions on the three surfaces are calculated and listed in Table 1. The $E_{ads}$ values in Table 1 indicate that Pb, Bi and Au prefer the hollow position on the (001) surface, Long-Bridge on the (110) surface and Bridge on the (111) surface. In addition, two adatoms prefer diagonal hollow positions (such as 1-site and 4-site or 2-site and 3-site) on the (001) surface with a $2 \times 2$ unit cell in Fig. 2(b). Five adatoms are most stable at high-symmetry hollow positions on the (001) surface with a $3 \times 3$ unit cell, as shown in Fig. 2(c). These lowest energy configurations with adsorbed atoms are utilized in the following analysis.

The $E_{ads}$ for adatoms (Pb, Bi and Au) and $E_{esp}$ for Fe atoms on the (001), (110) and (111) surfaces are listed in Table 2. For the (001) surface, the $E_{ads}$ for Pb and Bi with 1/4 ML coverage are consistent with previous calculations.[27] The calculations are also identical with $E_{ads}^{11l}$ for $2 \times 2 \times 11$ and $E_{ads}^{9l}$ for $3 \times 3 \times 9$ systems. As listed in Table 2, the $E_{ads}$ values of adatoms on the three surfaces are ordered by $E_{ads}(Bi) < E_{ads}(Pb) < E_{ads}(Au) < 0$. This indicates that Pb, Bi and Au atoms can be stably adsorbed on Fe surfaces from the liquid phase, and Bi is more stable than Pb and Au. In the case of the (001) surface, the $E_{esp}$ of surface Fe atoms with different coverages of adatoms increases in the order $E_{esp}(Pb) < E_{esp}(Bi) < E_{esp}(clean) < E_{esp}(Au)$. This indicates that Pb and Bi significantly accelerate the dissolution corrosion, while Au slightly mitigates the Fe atom escaping from the (001) surface. On (110) and (111) surfaces, the order of $E_{esp}(Pb) < E_{esp}(Bi) < E_{esp}(Au) < E_{esp}(clean)$ indicates that Pb, Bi and Au accelerate the dissolution corrosion, and show the same trend of corrosion capability as on the (001) surface.

As mentioned previously, the dissolution corrosion of liquid metals is affected by both the adsorption process and the escape process, and we have to consider the energetics in the two processes. $E_{ads}$ represents the possibility of adsorbing atoms from the liquid phase. The $E_{esp}$ related to surface stability determines the probability of formation of surface vacancies due to surface Fe atoms escape. Therefore, the possibility of adsorbed atoms $n_{ada}$, and vacancy (or escaped Fe) $n_{vac}$ can be simply expressed by $E_{ads}$ and $E_{esp}$, respectively,[9,16,17]

$$n_{ada} \propto A \times \exp\left(\frac{-E_{ads}}{kT}\right), \quad (3)$$

$$n_{vac} \propto B \times \exp\left(\frac{-E_{esp}}{kT}\right), \quad (4)$$

where $A$ and $B$ are constants depending on materials and environments. Herein, the higher the values of $E_{ads}$ and $E_{esp}$, the lower the possibility of adsorbed atoms and vacancies formed on the Fe surface. On the contrary, the lower $E_{ads}$ and $E_{esp}$ values represent a higher probability of adatoms and corrosion capability of liquid metal.

Since the adsorption possibility expressed by eqn (3) is not normalized, one can roughly evaluate the effect of adatoms by the ratio of vacancy probability ($n_{vac}$) in eqn (4) on the surfaces with adatoms to that on the clean Fe surface. For example, the ratio is 2.92 for Pb and 2.25 for Bi and 0.83 for Au adsorbed on the (001) surface with 1/4 ML coverage. This indicates that both adsorbed Pb and Bi accelerate dissolution corrosion on the clean (001) Fe surface, and the adsorbed Au slightly mitigates the corrosion. In the case of (110) and (111) surfaces, all the Pb, Bi and Au are found to accelerate the dissolution corrosion. However, the dissolution corrosion of liquid metals is affected by both adsorption and escape processes. The corrosion ability of liquid metals can be estimated by taking the probability of adsorption into account as $n_{ada-vac}$,

$$n_{ada-vac} = n_{ads} \times n_{vac} \propto A \times B \times \exp\left(\frac{-E_{ads} - E_{esp}}{kT}\right). \quad (5)$$

According to eqn (5), the ratios of $n_{ada-vac}$ for Pb to that for Bi and Au on the surfaces with different coverage are calculated by data in Table 2. Table 3 shows that the vacancy concentration on the three surfaces in liquid Pb is smaller than in liquid Bi,

Table 1 Adsorption energies ($E_{ads}$) of Pb, Bi and Au at different high-symmetry sites on the (001), (110) and (111) surfaces

| | $\theta$ | Pb | Bi | Au |
|---|---|---|---|---|
| H(001) | 1/4 | −0.75 (−0.72, ref. 27) | −1.36 (−1.31, ref. 27) | −0.52 |
| B(001) | 1/4 | −0.13 | −0.51 | 0.03 |
| T(001) | 1/4 | 0.10 | −0.12 | 0.54 |
| LB(110) | 1/4 | −0.91 | −1.16 | −0.47 |
| SB(110) | 1/4 | −0.75 | −1.10 | −0.15 |
| Top(110) | 1/4 | −0.71 | −0.91 | 0.20 |
| B(111) | 1/9 | −1.04 | −1.25 | −0.42 |
| T(111) | 1/9 | 0.57 | 0.65 | 0.84 |

Table 2 Adsorption energy ($E_{ads}$) of Pb, Bi and Au and escape energy ($E_{esp}$) of surface Fe atom on (001), (110) and (111) surfaces

| | $\theta$ | Clean | Pb | Bi | Au |
|---|---|---|---|---|---|
| $E_{ads}(001)$ | 1/4 | | −0.75 | −1.36 | −0.52 |
| $E_{esp}(001)$ | 1/4 | 5.81 | 4.74 | 5.00 | 6.00 |
| $E_{ads}^{11l}(001)$ | 1/4 | | −0.74 | −1.34 | −0.51 |
| $E_{ads}(001)$ | 1/2 | | −1.39 | −2.13 | −1.04 |
| $E_{esp}(001)$ | 1/4 | 5.81 | 5.30 | 5.74 | 6.03 |
| $E_{ads}(001)$ | 5/9 | | −3.55 | −4.87 | −2.62 |
| $E_{esp}(001)$ | 1/9 | 5.76 | 5.30 | 5.65 | 5.74 |
| $E_{ads}(001)$ | 1/9 | | −0.76 | −1.41 | −0.50 |
| $E_{esp}(001)$ | 1/9 | 5.76 | 4.80 | 5.04 | 5.97 |
| $E_{ads}^{9l}(001)$ | 1/9 | | −0.78 | −1.38 | −0.56 |
| $E_{ads}(110)$ | 1/9 | | −0.91 | −1.16 | −0.47 |
| $E_{esp}(110)$ | 1/9 | 6.19 | 5.29 | 5.33 | 5.33 |
| $E_{ads}(111)$ | 1/9 | | −1.04 | −1.25 | −0.42 |
| $E_{esp}(111)$ | 1/9 | 5.64 | 5.17 | 5.27 | 5.38 |

but larger than in liquid Au. The dissolution corrosion capability of liquid metals decreases in the order Bi > Pb > Au. This is consistent with experimental results, that Bi is more corrosive than Pb.[11,16,17,19]

The sequence of dissolution corrosion for liquid metals is further checked by surface properties, such as inter-layer distance, magnetic moments and charge density difference. The inter-layer distance, $d_{ij}$, is defined as the distance between the $i$th and $j$th atomic layers after structure relaxation. Correspondingly, the layer relaxation, $\Delta_{ij}$ is described by $\Delta_{ij} = (d_{ij} - d_0)/d_0$, where $d_0$ is the interplanar spacing in the bulk. In the case of the clean (001) surface with a $2 \times 2$ unit cell, the inter-layer distances in the top six layers are calculated to be $d_{12} = 1.39$ Å, $d_{23} = 1.46$ Å, $d_{34} \approx d_{45} \approx d_{56} \approx d_0 \approx 1.42$ Å. These lead to layer relaxations of $\Delta_{12} = -1.9\%$, $\Delta_{23} = 3.5\%$. These calculations are in good agreement with previous theoretical calculations[44,47–49] and experimental observations.[50] The local magnetic moments are calculated by projecting the wave functions onto the spherical harmonics within the spheres around each atom, with radii equal to the Wigner–Seitz radii. The magnetic moment is averaged to be 2.96 $\mu_B$ for surface Fe atoms and 2.26 $\mu_B$ for bulk Fe atoms. They are also consistent with previous calculations.[48,51] In the case of the liquid metal adsorbed surface, the inter-layer distance between first and second layer $d_{12}$ after relaxation increases by 8.2%, 8.8% and 1.2% for Pb, Bi and Au, respectively, compared to the value of 1.39 Å for the clean surface. The magnetic moment of the surface Fe atom is reduced from 2.96 $\mu_B$ to 2.76 $\mu_B$, 2.72 $\mu_B$ and 2.93 $\mu_B$ with Pb, Bi and Au adsorption, respectively. These hint that adsorbed Pb and Bi affect the Fe surface much more severely than Au, and the effect of Bi is slightly larger than that of Pb.

Table 3 The ratio of $n_{ada-vac}$ for Pb to Bi ($R_{Pb/Bi}$) and Au ($R_{Pb/Au}$), and for LBE to LGE ($R_{LBE/LGE}$), on the three surfaces with different coverage of adatoms ($\theta$(ada)) and vacancies ($\theta$(vac))

| | $\theta$(ada) | $\theta$(vac) | $R_{Pb/Bi}$ | $R_{Pb/Au}$ | $R_{LBE/LGE}$ |
|---|---|---|---|---|---|
| (001) | 1/4 | 1/4 | 0.70 | 4.44 | 1.38 |
| (001) | 1/2 | 1/4 | 0.74 | 2.94 | 1.32 |
| (001) | 5/9 | 1/9 | 0.38 | 3.97 | 1.40 |
| (001) | 1/9 | 1/9 | 0.66 | 4.18 | 1.38 |
| (110) | 1/9 | 1/9 | 0.81 | 1.62 | 1.20 |
| (111) | 1/9 | 1/9 | 0.90 | 2.29 | 1.16 |

The charge density difference, $\Delta\rho$, is defined by the following formula,[52]

$$\Delta\rho = \rho_{slab}^{ada} - \rho^{ada} - \rho_{slab}, \quad (6)$$

where $\rho_{slab}^{ada}$ is the total charge density of the slab with an adatom, and $\rho^{ada}$ and $\rho_{slab}$ are the charge densities of the adatom and clean slab, respectively. Negative values indicate a depletion of local electrons and positive values indicate an accumulation of local electrons. Fig. 4 shows the $\Delta\rho$ distribution of atoms around the interface from both side view and top view, corresponding to Fig. 3(b) and (c). It is noticed that there is an substantial rearrangement of electrons around the interface from various $\Delta\rho$ values. The upper panels of Fig. 4 show that $\Delta\rho$ around the adsorbed atoms is negative, and $\Delta\rho$ around Au is lower than that around Pb and Bi. This means the electrons around Au are depleted more severely than around Pb and Bi, and the bond strength of Au with the surface atoms is weaker than that of Pb and Bi. The negative $\Delta\rho$ area between Fe atoms at the top layer (Fe1) and the second layer (Fe2) indicates that electrons are depleted. This indicates that the bond strength between Fe1 and Fe2 is decreased. Clearly, the

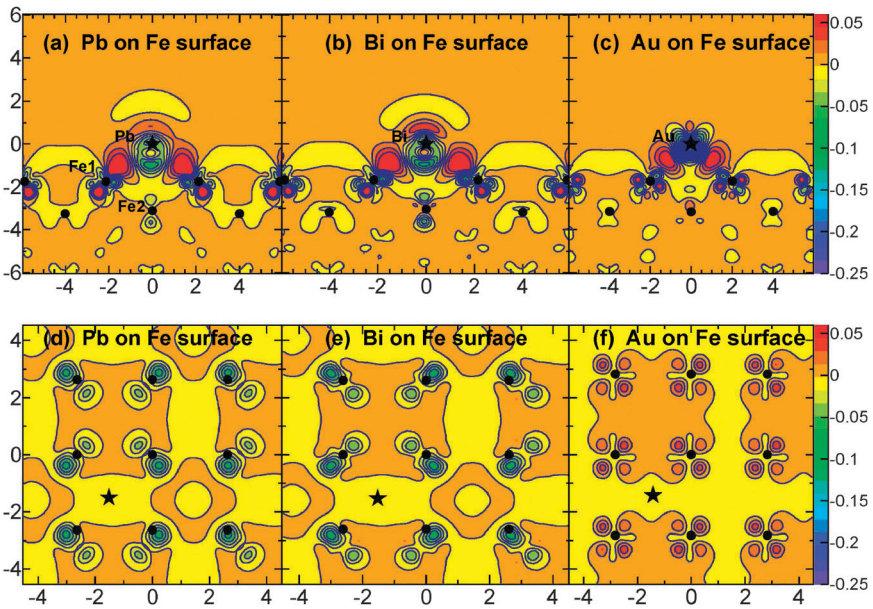


Fig. 4 Charge density difference around the interface from the side view (a–c) and top view (d–f). The black stars represent Pb on (a) and (d), Bi on (b) and (e), and Au on (c) and (f), respectively. The black dots are Fe atoms. The units are electrons per Å$^3$.

bond strength between Fe1 and Fe2 is significantly affected by adsorbed Pb or Bi, while not obviously affected by Au adsorption. The $\Delta\rho$ distributions on the lower panels show Pb and Bi make bond strength between Fe atoms on the surface weaken severely, while Au affects it slightly. These observations indicate that Pb or Bi not only degrade the interaction between Fe atoms at neighboring layers, but also decrease the bond strength between Fe atoms on the surface. The above results intuitively prove that the adatoms affect surface stability in the order Bi > Pb > Au.

Based on the above research for liquid metals, we explore complicated dissolution corrosion in liquid alloys, such as LBE and LGE. Considering experimental conditions, various chemical compositions and their proportions are implemented. According to recent experimental conditions at PSI, LBE consists of 45% Pb and 55% Bi, while LGE consists of 85% Pb and 15% Au. The vacancy concentration on the surface representing the corrosion capabilities of LBE and LGE can be simply accessed according to linear corrosion rate of the Pb and Bi(Au) activities,[11,18]

$$n^{\mathrm{LBE}}_{\mathrm{ada-vac}} = c^{\mathrm{LBE}}_{\mathrm{Pb}} \times n^{\mathrm{Pb}}_{\mathrm{ada-vac}} + c^{\mathrm{LBE}}_{\mathrm{Bi}} \times n^{\mathrm{Bi}}_{\mathrm{ada-vac}}, \quad (7)$$

$$n^{\mathrm{LGE}}_{\mathrm{ada-vac}} = c^{\mathrm{LGE}}_{\mathrm{Pb}} \times n^{\mathrm{Pb}}_{\mathrm{ada-vac}} + c^{\mathrm{LGE}}_{\mathrm{Au}} \times n^{\mathrm{Au}}_{\mathrm{ada-vac}}, \quad (8)$$

where $c^{\mathrm{LBE}}_{\mathrm{Pb}}$ or $c^{\mathrm{LGE}}_{\mathrm{Pb}}$ is the proportion of Pb in LBE or LGE, while $c^{\mathrm{LBE}}_{\mathrm{Bi}}$ and $c^{\mathrm{LGE}}_{\mathrm{Au}}$ represent the proportion of Bi and Au in LBE and LGE, respectively. According to the definitions eqn (7) and (8), the ratio of $n^{\mathrm{LBE}}_{\mathrm{ada-vac}}$ to $n^{\mathrm{LGE}}_{\mathrm{ada-vac}}$ is larger than that on the three surfaces as shown in Table 3. This indicates that the dissolution corrosion in LBE is slightly more severe than in LGE, which conflicts with experimental observations from PSI.[22] The conflict may be attributed to the fact that the observed corrosion is a mixture of oxidation and dissolution. The oxidation, such as magnetite and Fe–Cr spinel, may prevent Bi penetration, while allows Pb penetration from experimental observation.[8] However, the effects of oxidation have not yet been well understood without precise oxygen control, although oxygen content in LBE and LGE was estimated in the range $1 \times 10^{-8}$–$1 \times 10^{-6}$ wt%.[22] Therefore, oxygen effects are expected to be implemented in future theoretical studies.

### 3.2 Effect of alloying elements on the dissolution corrosion

Due to the degradation of steels inevitably caused by dissolution corrosion, researches are exploring efficient ways to prevent corrosion and ensure a long life time for steels in the ADS project. For this purpose, we first keep our eyes on the effect of alloying elements in popular steels on the dissolution corrosion. Nine alloying elements (Al, Si, V, Cr, Mn, Ni, Cu, Nb and Mo) are investigated through their effects on $E_{\mathrm{ads}}$ of adsorbed atoms and $E_{\mathrm{esp}}$ of surface Fe atoms.

The alloy-doped surface was constructed by substituting one surface Fe atom with an alloy atom on the optimized (001) surface with a 2 × 2 unit cell, as shown in Fig. 2(a). After relaxing the alloy-doped surface, we calculate the $E_{\mathrm{ads}}$ of adatoms and $E_{\mathrm{esp}}$ of surface Fe atoms on the relaxed alloy-doped surface, as listed in Table 4. On the clean alloy-doped surface, the $E_{\mathrm{esp}}$ of surface Fe atoms are increased by all of the alloys except Si and Ni, relative to 5.81 eV of $E_{\mathrm{esp}}$ on the clean pure surface. This indicates that dopants Si and Ni accelerate the escape of surface Fe atoms, and make the surface unstable in a vacuum. When a metal atom in the liquid phase is adsorbed on the alloy-doped surface, the most stable position for an adatom is firstly checked by comparing the total energies of the slab with the adatom at hollow, bridge and top positions. It is found that the hollow position is still the most stable position for the adatoms on all the alloy-doped surfaces, except for Pb on the Cr-doped surface, in which the bridge position is the most stable.

Table 4 $E_{\mathrm{ads}}$, $E_{\mathrm{esp}}$ and their sum ($E_{\mathrm{tot}}$) on the pure and alloy-doped surfaces

| | Clean | Pb | | | Bi | | | Au | | |
|---|---|---|---|---|---|---|---|---|---|---|
| Energy (eV) | $E_{\mathrm{esp}}$ | $E_{\mathrm{ads}}$ | $E_{\mathrm{esp}}$ | $E_{\mathrm{tot}}$ | $E_{\mathrm{ads}}$ | $E_{\mathrm{esp}}$ | $E_{\mathrm{tot}}$ | $E_{\mathrm{ads}}$ | $E_{\mathrm{esp}}$ | $E_{\mathrm{tot}}$ |
| Pure | 5.81 | −0.75 | 4.74 | 3.99 | −1.36 | 5.00 | 3.64 | −0.52 | 6.00 | 5.48 |
| Al | 6.03 | −0.51 | 5.12 | 4.61 | −1.07 | 5.39 | 4.32 | −0.43 | 6.15 | 5.72 |
| Si | 5.76 | −0.55 | 4.99 | 4.44 | −0.99 | 6.08 | 5.09 | −0.29 | 5.89 | 5.60 |
| V | 5.80 | −0.70 | 4.88 | 4.17 | −1.35 | 5.14 | 3.79 | −0.53 | 5.98 | 5.45 |
| Cr | 6.09 | −0.95 | 4.29 | 3.34 | −1.42 | 5.17 | 3.75 | −0.58 | 5.57 | 4.98 |
| Mn | 6.05 | −0.62 | 5.00 | 4.38 | −1.25 | 5.29 | 4.04 | −0.50 | 6.17 | 5.67 |
| Ni | 5.78 | −0.81 | 4.82 | 4.01 | −1.39 | 5.08 | 3.69 | −0.44 | 5.90 | 5.46 |
| Cu | 5.96 | −0.60 | 4.87 | 4.27 | −1.19 | 5.12 | 3.93 | −0.34 | 5.08 | 4.73 |
| Nb | 5.88 | −0.78 | 5.10 | 4.32 | −1.46 | 5.60 | 4.14 | −0.56 | 6.05 | 5.49 |
| Mo | 5.88 | −0.80 | 5.00 | 4.20 | −1.47 | 6.23 | 4.76 | −0.56 | 6.04 | 5.48 |

As shown in Table 4 and Fig. 5, some alloys enlarge $E_{\mathrm{ads}}$, representing a reduction in the adsorption probabilities of adatoms from the liquid phase. For example, Al, Si, V, Mn and Cu increase $E_{\mathrm{ads}}$ of Pb, while Al, Si, Mn and Cu enlarge $E_{\mathrm{ads}}$ of Bi, and Al, Si, Ni and Cu raise $E_{\mathrm{ads}}$ of Au. Correspondingly, they reduce the adsorption probabilities of Pb, Bi and Au on the

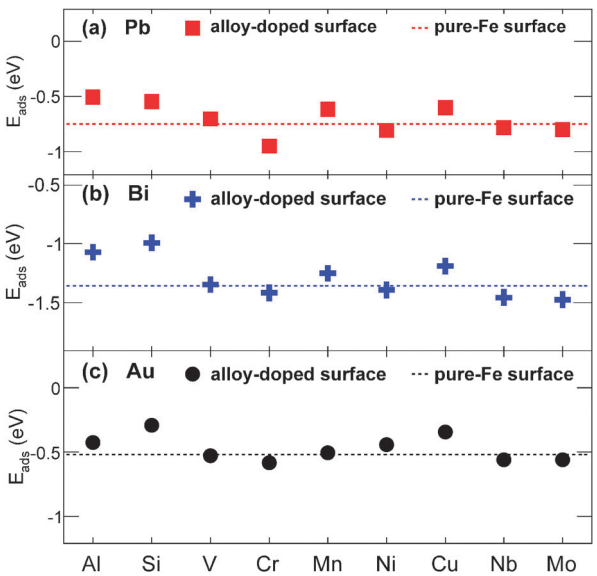


Fig. 5 Adsorption energies of Pb, Bi and Au on the alloy-doped surfaces are shown as red squares, blue crosses and black solid circles, respectively. The dashed lines show the adsorption energies of adsorbed atoms on the pure-Fe surface.

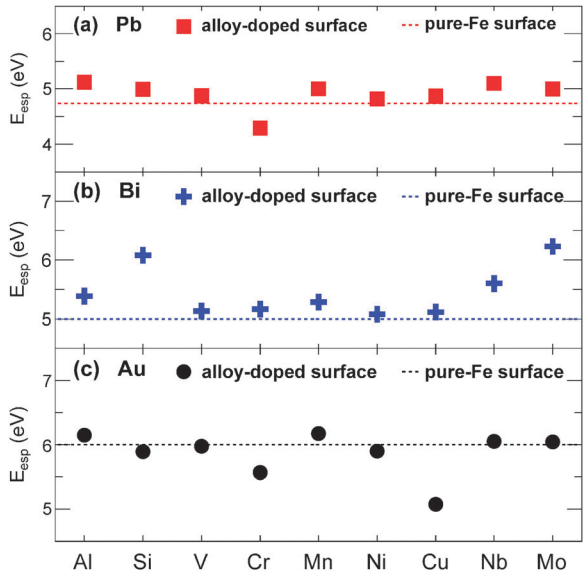


Fig. 6 Escape energies of Fe atoms (solid markers) on the alloy-doped surfaces and pure-Fe surfaces (dashed lines).

surface. However, some of the above alloys accelerate the escape of surface Fe atoms by reducing the $E_{esp}$ of surface Fe atoms, as shown in Fig. 6. For instance, Si and Cu promote the escape of surface Fe atoms from the surface with Au adsorption, and accelerate the dissolution corrosion of the Fe substrate in Au. To combine the two effects of the dissolution corrosion, we sum $E_{ads}$ and $E_{esp}$ on each alloy-doped surface as $E_{tot}$ and show them in Table 4 and Fig. 7. Relative to $E_{tot}$ for the pure Fe in Pb (3.99 eV), Bi (3.64 eV) and Au (5.48 eV), all the nine alloys can mitigate the dissolution corrosion of the Fe-substrate in liquid metals, except Cr in Pb, and Cr and Cu in Au. The alloys improving the Fe-substrate dissolution resistance

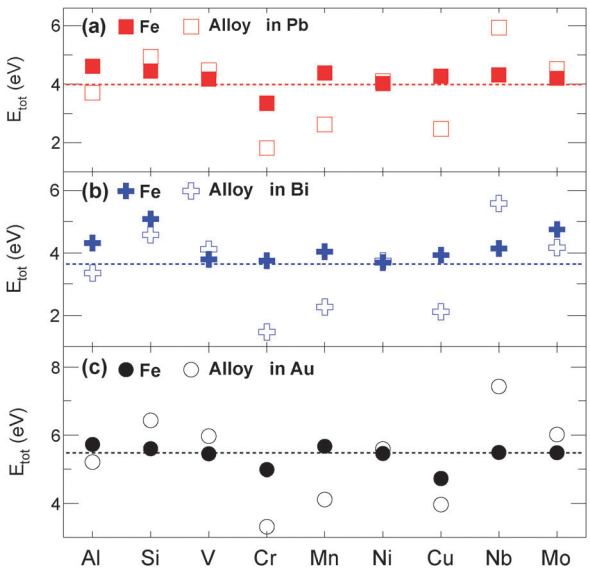


Fig. 7 Combination of adsorption and escape energies of Fe and alloy atoms on the alloy-doped (markers) and pure-Fe surfaces (dashed lines).

are ordered in Pb by Al > Si > Mn > Nb > Cu > Mo > V > Ni, in Bi by Si > Mo > Al > Nb > Mn > Cu > V > Cr > Ni, and in Au by Al > Mn > Si > Nb ~ Mo ≥ Ni ~ V. So far, Al shows the best protection for the Fe-substrate in Pb and Au, while Si is the best one to prevent the Fe-substrate dissolution corrosion in Bi.

Besides the above effects, the dissolution of alloys themselves also have to be considered, since they may be dissolved by liquid metals more easily than by surface Fe atoms. The escape energies for the surface doped alloys in liquid metals are calculated by the definition $E_{esp}(A) = E^{ada}_{slab-1} + E_A - E^{ada}_{slab-1+A}$, where $E_A$ is the energy of an isolated alloy atom, and $E^{ada}_{slab-1+A}$ is the energy of the alloy-doped slab. Similarly, the dissolution of surface alloys depends on the combination of the $E_{esp}(A)$ for the doped alloys and $E_{ads}$ for adsorbed atoms, *i.e.* $E_{tot}(A)$. As shown in Fig. 7, $E_{tot}(A)$ values of Cr, Mn and Cu are significantly lower than those of surface Fe atoms in liquid Pb, Bi and Au. This indicates that the three alloys have a lower dissolution resistance than Fe in the liquid metals without other complicate effects. This is consistent with experimental observations by mass transfer of twenty four various metals and alloys in liquid Pb.[11,53,54] Meanwhile, Al shows slightly worse dissolution resistance than Fe, and Si shows a similar dissolution resistance to Fe in liquid metals. The similarity between Si and Fe is consistent with Kurata's observations that the Si addition has no significant effect on the dissolution corrosion under low oxygen conditions.[55] However, Al and Si facing liquid metals containing oxygen exist as oxidations on the surface due to low chemical potential. These oxidations mitigate the dissolution corrosion, which has been experimentally proved by the low corrosion of Al-coating and Si-enriched steels (F82H, SX and SS316-Si) in liquid metals.[6,11,56–60] Therefore, other effects, such as oxidation and chemical reactions with impurities in steels, are required in our further studies to match the complicated experimental conditions.

## 4 Conclusion

In summary, energetic evaluation is used to investigate the dissolution corrosion capabilities of liquid metals on Fe(001), (110) and (111) surfaces using first principle calculations. Adsorption energies and escape energies are calculated to estimate the possibilities of adatoms (Pb, Bi and Au) and surface vacancies for escaping Fe atoms, respectively. The calculations indicate that the dissolution corrosion capabilities of liquid metals decrease in the order Bi > Pb > Au. The trend is independent of the preset surfaces with different coverages of adatoms and vacancies. This sequence is further proved by calculating the inter-layer distance, magnetic moments of surface Fe atoms and charge density difference around the interface. For liquid alloys such as LBE and LGE, the dissolution corrosion calculation takes all of the components into account, see eqn (7) and (8). The weighted vacancy concentrations of liquid alloys indicate that the dissolution corrosion of the bcc-Fe in LBE should be slightly more severe than in LGE.

Finally, the energetic method is developed to evaluate the effects of nine alloys in popular steels on the dissolution corrosion of alloy-doped surfaces. Cr accelerates the dissolution of surface Fe atoms in liquid Pb and Au, and Cu makes the dissolution corrosion severe in liquid Au. Meanwhile, Al, Cr, Mn and Cu doped on the surface show worse dissolution resistance than Fe in liquid metals. Therefore, the dissolution corrosion of martensite steels in liquid Pb, Bi and Au without oxygen (or with low oxygen concentration) may be mitigated by alloys, Si, V, Nb and Mo. This work develops an energetic method to evaluate the dissolution corrosion capabilities of liquid metals and select alloys with good corrosion resistance.

## Acknowledgements

This work was supported by the National Natural Science Foundation of China (No. 91026002, 91126002) and the Strategic Priority Research Program of Chinese Academy of Sciences (Grant No. KJCX2-YW-N35 and XDA03010303), and by the Center for Computation Science, Hefei Institutes of Physical Sciences.

## References

1 B. Gromov, Y. Belomitcev, E. Yefimov, M. Leonchuk, P. Martinov, Y. Orlov, D. Pankratov, Y. Pashkin, G. Toshinsky, V. Chekunov, B. Shmatko and V. Stepanov, *Nucl. Eng. Des.*, 1997, **173**, 207–217.
2 F. Groeschel, C. Fazio, J. Knebel, C. Perret, A. Janett, G. Laffont, L. Cachon, T. Kirchner, A. Cadiou, A. Guertin and P. Agostini, *J. Nucl. Mater.*, 2004, **335**, 156–162.
3 G. Bauer, *J. Nucl. Mater.*, 2010, **398**, 19–27.
4 M. Medarde, R. Moormann, R. Frison, R. Puźniak, E. Pomjakushina, K. Conder, E. Platacis, Y. Dai, D. Kiselev, L. Zanini, S. Török, P. Zagyvai, S. Heinitz, J. Neuhausen, D. Schumann and K. Thomsen, *J. Nucl. Mater.*, 2011, **411**, 72–82.
5 Y. Kurata and M. Futakawa, *Mater. Trans.*, 2007, **48**, 519–525.
6 Y. Kurata and S. Saito, *Mater. Trans.*, 2009, **50**, 2410–2417.
7 O. Yeliseyeva, V. Tsisar and G. Benamati, *Corros. Sci.*, 2008, **50**, 1672–1683.
8 L. Martinelli, F. Balbaud-Célérier, A. Terlain, S. Delpech, G. Santarini, J. Favergeon, G. Moulin, M. Tabarant and G. Picard, *Corros. Sci.*, 2008, **50**, 2523–2536.
9 C. Fazio, *et al.*, *Handbook on lead-bismuth eutectic alloy and lead properties, materials compatibility, thermal-hydraulics and technologies*, Isbn 978-92-64-99002-9. oecd/nea (organisation for economic cooperation and development/nuclear energy association) technical report, 2007.
10 C. Fazio, I. Ricapito, G. Scaddozzo and G. Benamati, *J. Nucl. Mater.*, 2003, **318**, 325–332.
11 J. Zhang, *Corros. Sci.*, 2009, **51**, 1207–1227.
12 I. Gorynin, G. Karzov, V. Markov and V. Yakovlev, *Met. Sci. Heat Treat.*, 1999, **41**, 384–388.
13 O. Kammerer, J. Weeks, J. Sadofsky, W. Miller and D. Gurinsky, *Trans. Metall. Soc. AIME*, 1958, **212**, 20–25.
14 J. Weeks and A. Romano, *Corrosion*, 1969, **25**, 131–136.
15 J. Weeks, *Nucl. Eng. Des.*, 1971, **15**, 363–372.
16 N. Li, *J. Nucl. Mater.*, 2002, **300**, 73–81.
17 J. Zhang and N. Li, *J. Nucl. Mater.*, 2008, **373**, 351–377.
18 G. Ilinčev, *Nucl. Eng. Des.*, 2002, **217**, 167–177.
19 J. Weeks, *Am. Soc. Metals, Trans. Quant.*, 1965, **58**, 302–322.
20 J. James and J. Trotman, *J. Iron Steel Inst.*, 1960, **194**, 319–323.
21 J. Konys, W. Krauss, Z. Voss and O. Wedemeyer, *J. Nucl. Mater.*, 2004, **329**, 1379–1383.
22 Y. Dai, W. Gao, T. Zhang, E. Platacis, S. Heinitz and K. Thomsen, *J. Nucl. Mater.*, 2012, **431**, 113–119.
23 E. Yamaki, K. Ginestar and L. Martinelli, *Corros. Sci.*, 2011, **53**, 3075–3085.
24 O. K. Chopra and P. F. Tortorelli, *J. Nucl. Mater.*, 1984, **123**, 1201–1212.
25 V. Ganesan, V. Ganesan and H. Borgstedt, *J. Nucl. Mater.*, 2003, **312**, 174–180.
26 D. Li, C. Song, H. Haiyan, C. Liu and B. Pan, *Phys. Chem. Chem. Phys.*, 2014, **16**, 7417–7422.
27 A. Legris, G. Nicaise, J.-B. Vogt and J. Foct, *J. Nucl. Mater.*, 2002, **301**, 70–76.
28 R. Li, M. Zhang and Y. Yu, *Appl. Surf. Sci.*, 2012, **258**, 6777–6784.
29 A. Bouzoubaa, B. Diawara, V. Maurice, C. Minot and P. Marcus, *Corros. Sci.*, 2009, **51**, 2174–2182.
30 B. L. Lü, G. Q. Chen, W. L. Zhou, H. Su and R. Liu, *J. Nucl. Mater.*, 2011, **418**, 286–291.
31 B. L. Lü, W. L. Zhou and G. Q. Chen, *Mater. Corros.*, 2012, **63**, 735–738.
32 B. L. Lü, G. Q. Chen, W. L. Zhou and H. Su, *Comput. Mater. Sci.*, 2013, **68**, 206–211.
33 Y. Ma and P. B. Balbuena, *J. Phys. Chem. C*, 2008, **112**, 14520–14528.
34 Y. Wang, P. Hu and X. Ma, *Phys. Chem. Chem. Phys.*, 2013, **15**, 17112–17117.
35 S. C. Yeo, S. S. Han and H. M. Lee, *Phys. Chem. Chem. Phys.*, 2013, **15**, 5186–5192.
36 G. Kresse and J. Hafner, *Phys. Rev. B: Condens. Matter*, 1993, **47**, 558–561.
37 G. Kresse and J. Furthmüller, *Phys. Rev. B: Condens. Matter*, 1996, **54**, 11169–11186.
38 J. P. Perdew, K. Burke and M. Ernzerhof, *Phys. Rev. Lett.*, 1998, **80**, 891.
39 G. Kresse and D. Joubert, *Phys. Rev. B: Condens. Matter Mater. Phys.*, 1999, **59**, 1758–1775.
40 P. E. Blöchl, *Phys. Rev. B: Condens. Matter*, 1994, **50**, 17953–17979.
41 H. J. Monkhorst and J. D. Pack, *Phys. Rev. B: Solid State*, 1976, **13**, 5188–5192.
42 P. K. Nandi, M. Valsakumar, S. Chandra, H. Sahu and C. Sundar, *J. Phys.: Condens. Matter*, 2010, **22**, 345501.
43 M. Levesque, M. Gupta and R. P. Gupta, *Phys. Rev. B: Condens. Matter Mater. Phys.*, 2012, **85**, 064111.
44 P. Błoński and A. Kiejna, *Vacuum*, 2004, **74**, 179–183.

 

45 S. Yu and J. Tobin, *Surf. Sci.*, 2007, **601**, L127–L131.
46 N. J. Bernstein, S. A. Akhade and M. J. Janik, *Phys. Chem. Chem. Phys.*, 2014, **16**, 13708–13717.
47 X. Yuan, C. Song, X. Kong, Y. Xu, Q. Fang and C. Liu, *Phys. B*, 2013, **425**, 42–47.
48 T. Shimada, Y. Ishii and T. Kitamura, *Phys. Rev. B: Condens. Matter Mater. Phys.*, 2010, **81**, 134420.
49 J. Jeon and B. Yu, *J. Korean Phys. Soc.*, 2011, **59**, 2291–2296.
50 Z. Wang, Y. Li, F. Jona and P. Marcus, *Solid State Commun.*, 1987, **61**, 623–626.
51 P. Błoński and A. Kiejna, *Surf. Sci.*, 2007, **601**, 123–133.
52 J. Park, B. Yu and H. Kim, *Phys. Rev. B: Condens. Matter Mater. Phys.*, 2009, **79**, 233407.
53 J. Cathcart and W. Manly, *Corrosion*, 1956, **12**, 43–47.
54 W. Manly, *Corrosion*, 1956, **12**, 46–52.
55 Y. Kurata, *J. Nucl. Mater.*, 2013, 401–408.
56 Y. Kurata, *J. Nucl. Mater.*, 2011, **415**, 254–259.
57 G. Benamati, P. Buttol, V. Imbeni, C. Martini and G. Palombarini, *J. Nucl. Mater.*, 2000, **279**, 308–316.
58 Y. Kurata, M. Futakawa and S. Saito, *J. Nucl. Mater.*, 2008, **373**, 164–178.
59 M. Kondo and M. Takahashi, *J. Nucl. Mater.*, 2006, **356**, 203–212.
60 G. Müller, A. Heinzel, J. Konys, G. Schumacher, A. Weisenburger, F. Zimmermann, V. Engelko, A. Rusanov and V. Markov, *J. Nucl. Mater.*, 2002, **301**, 40–46.